THE JOURNAL OF PHYSICAL CHEMISTRY C

Article

Cite This: J. Phys. Chem. C 2017, 121, 22787-22796

pubs.acs.org/JPCC

Molecular Dynamics Simulation of Resin Adsorption at Kaolinite Edge Sites: Effect of Surface Deprotonation on Interfacial Structure

T. R. Zeitler,[†] J. A. Greathouse,*[,‡] R. T. Cygan,[‡] J. T. Fredrich,[§] and G. R. Jerauld[§]

[†]Sandia National Laboratories, Carlsbad, New Mexico 88220, United States

[‡]Sandia National Laboratories, Albuquerque, New Mexico 87185-0754, United States

[§]BP America, P.O. Box 3092, Houston, Texas 77253, United States

ABSTRACT: Low-salinity water flooding, a method of enhanced oil recovery, consists of injecting low ionic strength fluids into an oil reservoir in order to detach oil from mineral surfaces in the underlying formation. Although highly successful in practice, the approach is not completely understood at the molecular scale. Molecular dynamics simulations have been used to investigate the effect of surface protonation on the adsorption of an anionic crude oil component on clay mineral edge surfaces. A set of interatomic potentials appropriate for edge simulations has been applied to the kaolinite (010) surface in contact with an aqueous nanopore. Decahydro-2-napthoic acid in its deprotonated form ($DHNA^-$) was used as a representative resin component of crude oil, with monovalent and divalent counterions, to test the observed trends in low-salinity water flooding experiments. Surface models include fully protonated (neutral) and deprotonated (negative) edge sites, which require implementation of a new deprotonation scheme. The surface adsorptive properties of the kaolinite edge under neutral and deprotonated conditions have been investigated for low and high $DHNA^-$ concentrations with Na^+ and Ca^{2+} as counterions. The tendency of $DHNA^-$ ions to coordinate with divalent (Ca^{2+}) rather than monovalent (Na^+) ions greatly influences adsorption tendencies of the anion. Additionally, the formation of net positively charged surface sites due to Ca^{2+} at deprotonated sites results in increased $DHNA^-$ adsorption. Divalent cations such as Ca^{2+} are able to efficiently bridge surface sites and organic anions. Replacing those cations with monovalent cations such as Na^+ diminishes the bridging mechanism, resulting in reduced adsorption of the organic species. A clear trend of decreased $DHNA^-$ adsorption is observed in the simulations as Ca^{2+} is replaced by Na^+ for deprotonated surfaces, as would be expected for oil detachment from reservoir formations following a low-salinity flooding event.

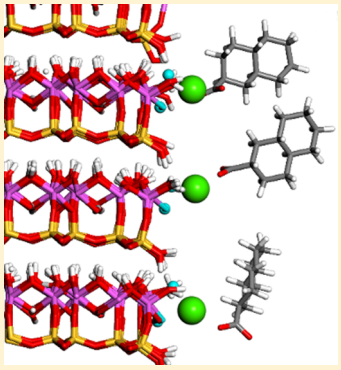

1. INTRODUCTION

In order to improve oil field production, a number of enhanced oil recovery (EOR) technologies have been developed. One successful technique involves injecting low-salinity water into oil reservoirs, resulting in increased recovery of oil compared to conventional flooding techniques.[1] While the exact mechanism of increased production following low-salinity flooding is not completely known, several explanations have been proposed[2,3] to describe increased oil detachment from the underlying rock formation after the introduction of low-salinity fluids. A description of the surface interactions that affects the wettability of oil under these conditions is of great economic interest.

The impact of low-salinity flooding is greatly enhanced in the presence of phyllosilicate phases such as clay minerals.[4] Clay minerals, including smectites and kaolinite, are highly anisotropic layered materials commonly found in petroleum reservoirs. These aluminosilicate minerals have a high propensity for adsorbing water, aqueous ions, and the hydrophilic components of crude oil. Importantly, Jerauld et al.[2] showed that a linear relationship exists between kaolinite content in the reservoir rock and incremental oil recovery during low-salinity flooding.

Molecular modeling studies have been used to investigate the adsorptive properties of clay minerals, primarily focusing on basal surface adsorption of aqueous ions, including, for example, radionuclide contaminants.[5−8] A limited number of studies have focused on the adsorption of crude oil components on the pH-independent basal surface of clay phases, using classical molecular dynamics (MD) simulations[9,10] and quantum methods.[10] However, pH-dependent edge surfaces likely play a key role in the observed trends in controlled water flooding experiments.[1−3] The basal and edge surfaces have significantly different properties that depend on the pH and salinity of aqueous solutions in contact with their surfaces. Several simulation studies of clay edge surfaces have been completed but primarily on small systems using electron structure methods based on density functional theory (DFT).[11−16] Atomic-scale simulations have typically lacked force field potentials to accurately simulate clay mineral edge surfaces (with some recent exceptions[17−19]), particularly a set of edge surface parameters that are transferrable and compatible with bulk and basal surface models.

One previous modeling study has investigated low-salinity flooding by considering the adsorption of organics to the basal

Received: July 7, 2017
Revised: September 15, 2017
Published: October 5, 2017

DOI: 10.1021/acs.jpcc.7b06688
J. Phys. Chem. C 2017, 121, 22787−22796

(not edge) surface of a common smectite clay montmorillonite.[9] Effects of solution pH were studied by changing the deprotonation state of the organic but not that of the clay mineral surface. The main difference between this previous study and the simulations of this study is that organics in the previous work were allowed to redistribute in the pore prior to solvation, which led to so-called "oil-wet" initial surface conditions. Here, the equilibration of organics occurs in the presence of water, allowing for a distribution of organics at the surface that is dependent on the aqueous and surface interactions.

The present work follows from our recent simulation study of crude oil adsorption onto basal (pH-independent) clay surfaces, in which organic adsorption was controlled primarily by hydrophobic interactions rather than changes in solution salinity.[10] Our current focus is on kaolinite, the main clay component in sandstone reservoirs and directly linked to low-salinity oil recovery.[2] While adsorption trends on the basal surfaces of kaolinite have now been established,[10] we can examine salinity effects on adsorption at pH-dependent edge sites. We apply a set of interatomic potentials[17] appropriate for clay edge simulations to the kaolinite (010) surface in contact with aqueous nanopores including a crude oil component. The (010) edge surface of kaolinite is predicted to be one of the predominant types of kaolinite edge surfaces[20,21] and has been previously studied for that reason via molecular simulation.[13] Decahydro-2-napthoic acid[22] in its deprotonated form ($DHNA^-$) was used as a representative resin component of crude oil and involves monovalent and divalent counterions to test the observed trends in low-salinity water flooding experiments. Relatively high pH conditions expected in petroleum reservoirs (pH > 6) were modeled by imposing a negatively charged deprotonated surface. Adsorption of $DHNA^-$ on the deprotonated kaolinite (010) edge surface was subsequently examined. The surface complexes that were formed during the MD simulations have not been entirely characterized since the focus of this study is an explanation for the larger-scale adsorption phenomenon; however, it is recognized that the structures of these complexes could be used as starting points for additional detailed studies.

2. SIMULATION METHODS

2.1. Edge Surface Model. A bulk kaolinite ($Al_2Si_2O_5(OH)_4$) model was created from an orthogonalized 8 × 5 × 3 supercell with atomic positions based on experimentally derived structural parameters.[23] A MD simulation was performed as an *NPT* ensemble (number of particles *N*, pressure *P*, temperature *T*) with the Clayff force field[24] to derive relaxed cell lengths (41.60 × 44.67 × 21.51 Å). The orthogonalized unit cell model was created with appropriate cell lengths (5.20 × 7.17 × 8.93 Å, where *b* and *c* axes were switched so that the *c* axis included the interface and nanopore region).

An orthogonal (010) edge surface model was created with the Materials Studio software package (BIOVIA, Inc.), using a 2 × 1 × 1 supercell and a vacuum introduced in the *c*-direction, resulting in cell lengths of 10.40 × 7.17 × 82.15 Å. Surface Al atoms are identical (five-coordination, including a single OH group). Surface Si atoms are four-coordinated on one side of the cell (with a nonbridging O atom) and three-coordinated on the other. To create two identical surfaces, one H atom was added to the nonbridging O (creating an OH group), and an OH group was added on the three-coordinated Si (effectively, a neutral water molecule is added and split, Figure 1). No charge redistribution was necessary to create two neutral edge surfaces. From this structure, a supercell was created that is 8 × 5 × 6 relative to the original structure (i.e., six layers) with cell lengths 41.60 × 43.02 × 82.15 Å. Each kaolinite surface has an area of 17.9 nm^2 and surface OH density of 5.36 OH·nm^{-2}.

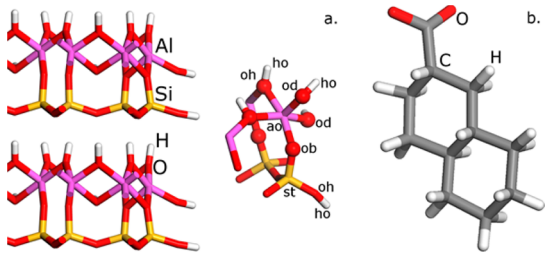

Figure 1. (a.) Kaolinite (010) edge surface models (Al, Si, O, and H atoms are represented by purple, yellow, red, and white sticks, respectively), indicating atom types for a deprotonation site at Al (abstraction of the surface on the right). (b.) Resin model ($DHNA^-$).

Table 1. Kaolinite Force Field Parameters[a]

Nonbond[b]: $E_{nonbond} = \frac{q_i q_j}{r} + 4\varepsilon_{ij}\left[\left(\frac{\sigma_{ij}}{r}\right)^{12} - \left(\frac{\sigma_{ij}}{r}\right)^{6}\right]$				
species	atom type	q/e	σ (Å)	ε (kcal·mol^{-1})
tetrahedral silicon	st	2.1000	3.3020	1.8405×10^{-6}
octahedral aluminum	ao	1.5750	4.2712	1.3298×10^{-6}
bridging oxygen	ob	−1.0500	3.1655	0.1554
hydroxyl oxygen	oh	−0.9500	3.1655	0.1554
hydroxyl hydrogen	ho	0.4250	0.0000	0.0000
water oxygen	o*	−0.8200	3.1655	0.1554
water hydrogen	h*	0.4100	0.0000	0.0000
hydroxyl oxygen (deprotonated water)	od[c]	−1.1875	3.1655	0.1554
aqeuous sodium ion	Na	1.0	0.1301	2.3500
aqueous calcium ion	Ca	2.0	0.1000	2.8720
Bond Stretching: $E_{bond} = k(r - r_0)^2$				
bond	k (kcal·mol^{-1}·Å^{-2})	r_0 (Å)		
o*−h*	553.9350	1.0000		
Bond Stretching[d]: $E_{bond} = D_0[1 - e^{-\alpha(r-r_0)}]^2$				
bond	D_0 (kcal·mol^{-1})	α (Å^{-1})	r_0 (Å)	
oh−ho	132.2491	2.1815	0.9450	
od−ho	132.2491	2.1815	0.9450	
Bonded Angle Bend: $E_{angle} = k(\theta - \theta_0)^2$				
angle	k (kcal·mol^{-1}·rad^{-2})	θ_0 (deg)		
h*−o*−h*	45.7696	109.47		
Nonbond Angle Bend (NB3B)[e]: $E_{angle} = k(\theta - \theta_0)^2$				
angle	k (kcal·mol^{-1}·rad^{-2})	θ_0 (deg)		
st−O−H[f]	6.35	120.0		
ao−O−H[f]	6.35	120.0		

[a] q_i is the atomic charge on atom *i*, $\sigma_{ij} = \sqrt{\sigma_i \sigma_j}$ and $\varepsilon_{ij} = \sqrt{\varepsilon_i \varepsilon_j}$ represent the van der Waals radius and energy well depth for the atomic pair, *r* is the interatomic distance, D_0 is the depth of the bond potential well, α is related to the width of the bond potential energy curve, r_0 is the equilibrium bond distance, *k* is the angle bend force constant, and θ_0 is the equilibrium angle. [b]Reference 24. A potential cutoff of 10 Å was used. [c]First used in current work. The Al−O cutoff is 2.8 Å, and the O−H cutoff is 1.2 Å. [d]Reference 25. [e]Reference 17. [f]Applies to edge and layer hydroxyl groups in kaolinite.

DOI: 10.1021/acs.jpcc.7b06688
J. Phys. Chem. C 2017, 121, 22787−22796

Table 2. Model Details, Including Cell Lengths (Å), Adsorbate Concentration, and Counterion Concentration

model	simulation	*a*	*b*	*c*[a]	surface charge (e·nm^{-2})	#H_2O	#DHNA$^-$	#Ca	#Na	#deprotonated H_2O
					Neutral					
1	pure H_2O	41.6	43.0	79.0	0	3332	0	0	0	
2	dhna14ca7	41.6	43.0	81.1	0	3332	14	7	0	
3	dhna28ca14	41.6	43.0	83.4	0	3332	28	14	0	
4	dhna14na14	41.6	43.0	81.3	0	3332	14	0	14	
5	dhna28na28	41.6	43.0	83.4	0	3332	28	0	28	
6	dhna14ca7−2xh2o	41.6	43.0	136.9	0	6664	14	7	0	
					Charged					
7	ca6dp12	41.6	43.0	79.0	−0.335	3320	0	6	0	12
8	na12dp12	41.6	43.0	79.3	−0.335	3320	0	0	12	12
9	dhna14ca13dp12	41.6	43.0	81.3	−0.335	3320	14	13	0	12
10	dhna28ca20dp12	41.6	43.0	83.2	−0.335	3320	28	20	0	12
11	dhna14na26dp12	41.6	43.0	81.2	−0.335	3320	14	0	26	12
12	dhna28na40dp12	41.6	43.0	84.6	−0.335	3320	28	0	40	12
13	dhna14ca4na18dp12	41.6	43.0	80.9	−0.335	3320	14	4	18	12
14	dhna14ca8na10dp12	41.6	43.0	81.4	−0.335	3320	14	8	10	12
15	dhna14ca11na4dp12	41.6	43.0	81.2	−0.335	3320	14	11	4	12

[a]Following *NPT* step.

2.2. Resin Model. The deprotonated form of the decahydro-2-napthoic acid molecule (DHNA$^-$) was examined as a representative resin phase. DHNA$^-$ ions were modeled using CVFF force field parameters.[26] Complete force field details for DHNA$^-$ are given in a previous paper.[10] Both Na^+ and Ca^{2+} were used as solution-based counterions, with parameters given in Table 1.

2.3. Simulation Types. For each simulation, the vacuum gap (pore space) between the edge surfaces of the periodic cell was filled with water molecules to achieve the appropriate bulk water density. The first simulation included no adsorbates. Fourteen additional model systems were simulated, which included DHNA$^-$ ions as adsorbates and Na^+ or Ca^{2+} as counterions (Table 2). Six of the simulations involved neutral surfaces, and nine incorporated deprotonated surfaces.

2.4. Deprotonation Scheme. At the near-neutral pH found in petroleum reservoirs, the deprotonation of kaolinite edges is expected based on experimental[27] and DFT[28] pK_a data. As described in Table 1, surface OH groups were tethered to Al or Si atoms using a nonbonded harmonic angle bend potential developed for Mg−O−H edge sites.[17] Water molecules that were coordinated to surface Al were not explicitly tethered to individual sites but were exchangeable with "bulk" water (there is no distinction between these two types of water). To model a deprotonated edge, H_2O molecules that were associated with selected edge Al were "deprotonated" to become OH groups, so that two OH groups were associated with each of those selected edge Al (Figure 2); a H_2O molecule was removed from the bulk H_2O and an OH was added. The charge on both of the OH groups—they are now indistinguishable as far as which was previously part of a H_2O molecule—was adjusted by increasing the charge on the O atom from −0.95 *e* to −1.1875 *e* in order to result in a charge of −1 *e* at each site. Counterions of integral charge were added to maintain charge neutrality over the entire model. A maximum of one surface Al per layer was designated as a deprotonation site (i.e., has two OH groups). Deprotonation sites in adjacent layers were separated from each other. With the addition of 12 deprotonation sites, the surface coverage of Al−OH increased from 2.68 to 3.02 OH·nm^2; there remained 2.68 Si−OH·nm^2. The deprotonation sites were chosen as "H_2O at Al" sites based on experimental evidence.[29]

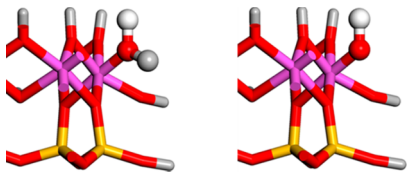

Figure 2. Deprotonation scheme: H atom is removed from H_2O coordinated to Al (left), resulting in a second OH group on Al at the deprotonation site (right).

2.5. Molecular Dynamics Details. The LAMMPS[30] code was used for all MD calculations. Kaolinite phases were modeled using mostly nonbonded (Lennard-Jones short-range and Coulombic long-range) interactions using parameters from Clayff.[24] A Morse potential was used for the O−H bond stretch in the kaolinite structure to improve upon the simple harmonic potential incorporated in the original Clayff parameter set.[25] A recently developed nonbonded three-body harmonic potential was used for all Al−O−H and Si−O−H interactions in the kaolinite structure.[17] The flexible SPC model was used for water, which includes a harmonic O−H bond stretch and H−O−H angle bend terms.[31] To prevent the independent translation of kaolinite layers, three atoms (Al and Si) in the center of each kaolinite layer were constrained throughout all simulation steps. Organic anions and counterions were initially placed at the center of the simulation cell in the middle of the nanopore.

Simulations consisted of the six steps shown in Table 3. First, water and any adsorbates and/or counterions were simulated at 1000 K to allow for mixing while keeping the kaolinite structure fixed. The unconstrained atoms were subsequently cooled to 300 K. All atoms were then allowed to move, and an *NPT* ensemble was used to allow for relaxation of the simulation cell in the *c*-direction (perpendicular to the kaolinite surface). Water and any organic anions and/or counterions were simulated again at 1000 K in the *NVT* (volume *V*) ensemble. In this step, 20 individual structures were output for use in subsequent simulation steps. Step 5 consisted of cooling the mobile atoms to 300 K in each of the 20 replicate simulations.

DOI: 10.1021/acs.jpcc.7b06688
J. Phys. Chem. C 2017, 121, 22787−22796

Table 3. MD Simulation Details

step	mobile	ensemble	temp (K)	time
1	H_2O, organics	*NVT*	1000	100 ps
2	H_2O, organics	*NVT*	1000−300	100 ps
3	All*	*NPT*	300	1 ns
4[a]	H_2O, organics	*NVT*	1000	100 ps
5	H_2O, organics	*NVT*	1000−300	100 ps
6[b]	All[c]	*NVT*	300	4 ns

[a]Output 20 starting configurations for step 5 input. [b]Statistics collected over the final 2 ns. [c]Three Al or Si atoms pinned per layer at all times.

Finally, all atoms were allowed to freely move (except three fixed to prevent layer translation, as noted above), and structural data were collected over the last 2 ns of simulation time and averaged over the 20 independent simulations.

3. RESULTS

Structural features of the kaolinite edge in contact with pure water (Model 1, no adsorbates or counterions) provide a baseline assessment of the surface model behavior. The coordination shells of surface Al (six-coordinated) and Si (four-coordinated) were satisfied throughout this simulation (Table 4). While the initial surface Al coordination was five for the as-created surface, the coordination number reached nearly six following equilibration due to coordination with water molecules. The final Al coordination consists of two "internal OH" (which connect Al to Al), two "bridging oxygens" (which connect Si to Al), one surface OH group, and one water molecule. For Si, the coordination consists of three bridging oxygens (which connect to Si and Al) and one surface OH group. The first peak of the surface Al−O(H) radial distribution function (RDF) is at a separation of 1.85 Å, in good agreement with previous DFT-calculated separations of 1.833−1.863 Å at pyrophyllite (010) edges in contact with water.[11,12,15] Similarly, the surface Si−O(H) separation is 1.58 Å, slightly smaller than the DFT values (1.64−1.650 Å).[14,15,18]

3.1. Neutral Surface Adsorption. Five model systems were simulated with a neutral ("protonated") kaolinite surface and $DHNA^-$ ions in solution (Table 2, Models 2−6). Two $DHNA^-$ concentrations were studied, with two types of counterions (Na^+ and Ca^{2+}) tested for each concentration. An expanded aqueous pore with reduced $DHNA^-$ concentration (Model 6) was tested with Ca^{2+} counterions. One-dimensional (1D) atomic density profiles (Figure 3) show the ordering of ionic species near neutral and deprotonated surfaces for representative nanopore compositions. Representative snapshots for the neutral surfaces are shown in Figure 4. A summary of adsorption results for all model systems is given in Table 5.

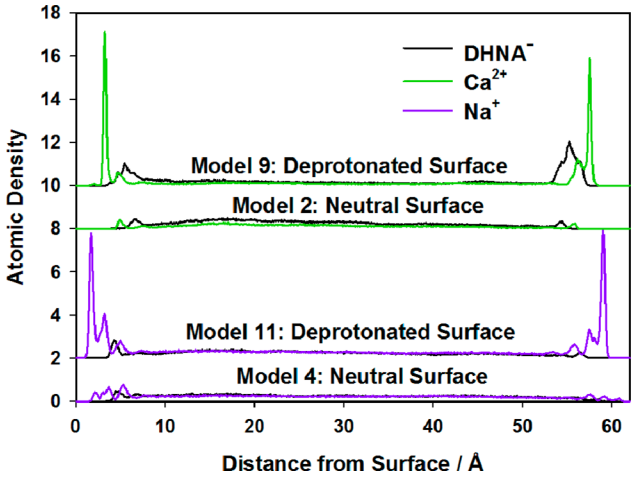

Figure 3. Atomic density profiles of $DHNA^-$, Ca^{2+}, and Na^+ for neutral and deprotonated surfaces. $DHNA^-$ densities were determined from positions of carboxylate C atoms.

For systems with Ca^{2+} on a neutral surface, surface adsorption was observed for both species beginning at about 5 Å from the surface; the surface is defined by the peak in the surface Al density (Figure 3). Adsorption of $DHNA^-$ is seen on both surfaces, typically with Ca^{2+} "bridging" the carboxylate group to the surface; the Ca^{2+} density profile shows a peak closer to the surface than the $DHNA^-$ plot (Model 2, Figure 4). Areas under peaks in the 1D atomic density profiles indicate an average surface coverage of 1.1 $DHNA^-$ and 0.52 Ca^{2+} ions. Desorbed Ca^{2+} ions occur near carboxylate groups, sometimes bridging multiple $DHNA^-$ ions. The coordination environment for adsorbed Ca^{2+} is discussed below. The cutoff for identifying surface adsorption is determined by the minimum in the density profile (at around 6−7 Å from each surface). Surface coverage results are summarized in Table 5.

The density profile for Na^+ is somewhat different from that of Ca^{2+} due to the tendency of the former to form inner-sphere surface complexes (Model 2, Figure 3). Adsorbed Na^+ is found without coordinating $DHNA^-$ at both the surface and in the bulk, which is different from the observed Ca^{2+} behavior (Figure 4). Some asymmetry is seen in the density plots incorporating the entire nanopore, especially for $DHNA^-$, likely an effect of averaging density profiles from 20 separate MD simulations.

3.2. Deprotonated Surface Adsorption. Nine model systems were simulated with a charged ("deprotonated") kaolinite surface (Table 2, Models 7−15). A deprotonated surface was created according to the scheme described above,

Table 4. Oxygen Coordination Numbers for Surface Al and Si for Models 1 (Pure H_2O Simulation) and 7 (6 Ca^{2+}, 12 dpH_2O) Based on a Metal−Oxygen Cutoff of 3.0 Å

surface metal	model	internal OH	bridging O	surface OH [Al]	surface OH [Si]	water	total
Al[a]	1	2.00	2.00	1.00	0.00	0.97	5.97
	7	1.99	1.90	1.04	0.03	0.78	5.74
Al(d)[b]	1						
	7	1.68	1.47	2.00	0.00	0.02	5.17
Si	1	0.01	3.00	0.00	1.00	0.01	4.01
	7	0.01	3.00	0.00	1.00	0.01	4.02

[a]Al at a nondeprotonation site. [b]Al at a deprotonation site.

DOI: 10.1021/acs.jpcc.7b06688
J. Phys. Chem. C 2017, 121, 22787−22796

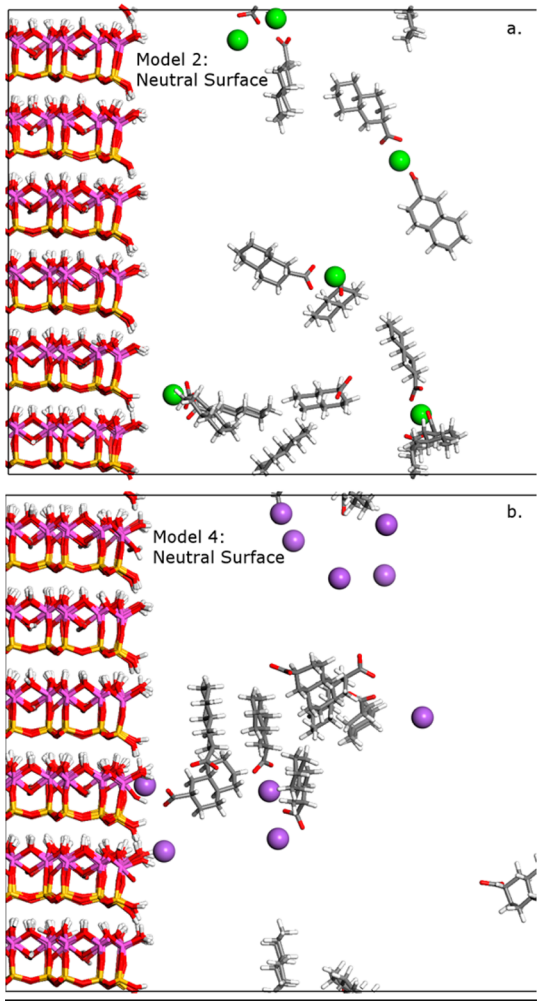

Figure 4. Representative structure snapshots of (a) Model 2 (14 $DHNA^-$, 7 Ca^{2+} ions) and (b) Model 4 (14 $DHNA^-$, 14 Na^+ ions). Water molecules are not displayed in the pore region for ease in viewing organic anions and counterions.

resulting in a negatively charged surface. In each case, there were 12 deprotonation sites ($-Al(OH)_2^-$), and the net charge of the kaolinite framework was -12 *e*. For simulations of $DHNA^-$ near the negatively charged surfaces, counterions were included in the pore to compensate for negative charge due to surface deprotonation and $DHNA^-$. The charge-balancing Ca^{2+} and Na^+ ions were present with and without $DHNA^-$.

Charge-balancing Ca^{2+} and Na^+ ions were found to adsorb at the surface sites. Increased $DHNA^-$ adsorption was observed compared to the neutral surfaces, with some adsorption occurring closer to the surface (Models 9 and 11, Figure 3). The coordination environments of adsorbed cations are quantified via RDF analysis below (Table 6).

Table 6. Cation Coordination Numbers for Neutral and Charged Surfaces (with and without $DHNA^-$ Present) Based on a Metal−Oxygen Cutoff of 3.0 Å

cation	model	type	surface	water	$DHNA^-$	total
Ca	2	neutral	0.00	4.53	3.47	7.99
	7	charged	1.48	5.95		7.43
	9	charged with $DHNA^-$	1.00	4.77	1.93	7.70
Na	4	neutral	0.17	4.87	0.69	5.73
	8	charged	1.96	3.83		5.79
	11	charged with $DHNA^-$	1.23	4.13	0.43	5.79

From atomic density plots, we note that the local structure at Al sites on the neutral surface (Figure 5a) is nearly identical to neutral Al edge sites on the negatively charged surface (Figure 5b). However, the local environment near a deprotonated Al site with two surface OH groups is different from a nonprotonation surface Al site with only one surface OH group (Figure 5c). There are multiple density peaks for deprotonated Al(d) sites away from the surface, indicating that Al at those sites extends into the aqueous region by as much as 2 Å. Because these peaks are well-defined and no Al is found in solution, we conclude that the distorted Al sites are stable during the simulation. Because the Al at deprotonation sites extends from the surface, there are fewer coordinating "internal OH" and bridging O (while the increase due to water coordination is relatively small due to the existence of two

Table 5. Surface Coverage Results

model	simulation	%$DHNA^-$ on surface	%Ca on surface	%Na on surface	average #$DHNA^-$ on surface	average #Ca on surface	average #Na on surface	$DHNA^-$/ cation on surface	$DHNA^-$/ deprotonation
Neutral									
1	pure H_2O								
2	dhna14ca7	8.1	7.4		1.13	0.52		2.17	
3	dhna28ca14	3.8	4.5		1.07	0.64		1.69	
4	dhna14na14	4.8		18.9	0.67		2.64	0.25	
5	dhna28na28	5.9		12.6	1.65		3.54	0.47	
6	dhna14ca7−2xh2o	1.6	1.9		0.22	0.13		1.67	
Charged									
7	ca6dp12		90.9			5.45			
8	na12dp12			70.7			8.49		
9	dhna14ca13dp12	45.3	62.4		6.34	8.11		0.78	0.53
10	dhna28ca20dp12	12.6	22.3		3.53	4.46		0.79	0.29
11	dhna14na26dp12	7.9		47.0	1.10		12.21	0.09	0.09
12	dhna28na40dp12	4.7		34.3	1.31		13.70	0.10	0.11
13	dhna14ca4na18dp12	14.0	24.9	49.0	1.96	1.00	8.83	0.20	0.16
14	dhna14ca8na10dp12	16.2	48.4	53.9	2.27	3.87	5.39	0.24	0.19
15	dhna14ca11na4dp12	34.6	58.5	52.7	4.85	6.44	2.11	0.57	0.40

DOI: 10.1021/acs.jpcc.7b06688
J. Phys. Chem. C 2017, 121, 22787−22796

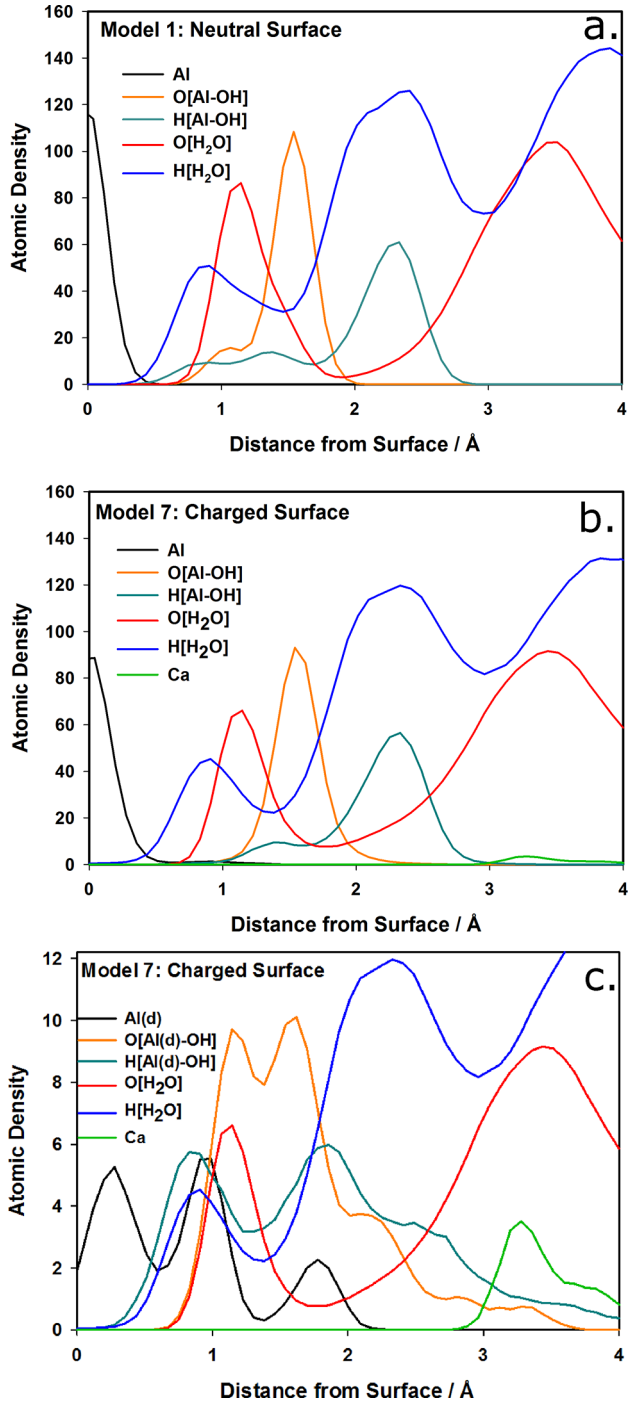

Figure 5. Comparison of atomic density profiles for atoms near Al at (a) a neutral surface (Model 1), (b) neutral $-Al(OH)(OH_2)$ sites on a deprotonated surface (Model 7), and (c) deprotonated $-Al(OH)_2$ sites (Model 7) (O and H profiles for water are scaled in (c) to 10% of the values in (a) and (b)).

coordinating hydroxyl groups), resulting in an overall reduction in coordination (Table 4).

Models 9 and 11 serve as end points in a series of varying Ca^{2+}/Na^+ ratios (13:0 and 0:26, respectively). Three additional models were created with a range of Ca^{2+}/Na^+ ratios between these end points but with a fixed $DHNA^-$ concentration (14 ions). The amount of adsorbed $DHNA^-$ decreased as the Na^+ concentration in the pore increased (Figure 6).

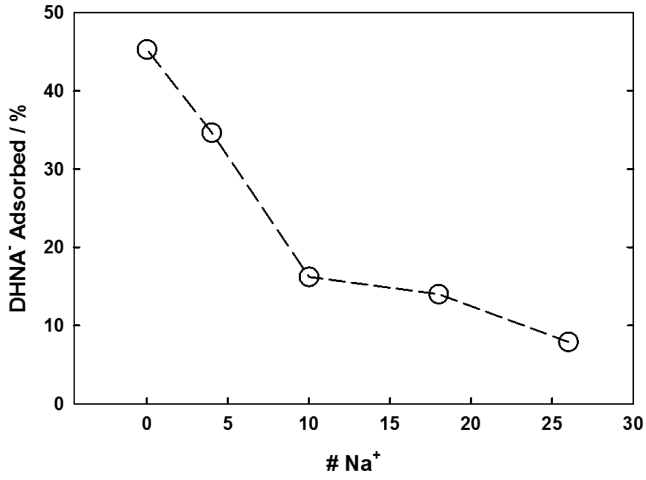

Figure 6. $DHNA^-$ adsorption with Na^+ content for models with 14 $DHNA^-$ and 12 deprotonated H_2O (charge compensation provided by Na^+ and Ca^{2+} ions).

4. DISCUSSION

For neutral surfaces (Models 1−6), when Na^+ ions were used as counterions instead of Ca^{2+}, the surface coverage of $DHNA^-$ decreased from 1.1 in the Ca^{2+} case to 0.67 ions, despite the Na^+ coverage increasing from 0.52 Ca^{2+} to 2.64 Na^+. These differences indicate that Ca^{2+} is more effective at binding $DHNA^-$ to the surface via cation bridging; compare the $DHNA^-$/ion ratios of 2.2 for Ca^{2+} and 0.25 for Na^+. Divalent cations are able to coordinate multiple anions, or in this case one anion and one surface site. The first Na^+ peak in the atomic density profile (1.87 Å) is approximately 3 Å closer to the surface than the first Ca^{2+} peak (Models 2 and 4, Figure 3). These results are consistent with those for MD simulations of adsorption of $DHNA^-$ with Na^+ and Ca^{2+} onto the basal surface of kaolinite.[10]

When the concentration of $DHNA^-$ was doubled near the neutral surface containing Ca^{2+} ions, adsorption of $DHNA^-$ and Ca^{2+} was essentially unchanged, with average surface coverages of 1.1 and 0.64, respectively. We can conclude that the upper limit of $DHNA^-$ adsorption on these edge surfaces is quite low despite an excess of $DHNA^-$ in the aqueous region. The formation of Ca-bridged $(DHNA^-)_2$ dimers (Figure 4a) prevents additional adsorption.

Doubling the $DHNA^-$ concentration in the presence of Na^+ ions nearly doubles the surface coverage of both $DHNA^-$ (0.7 to 1.7) and Na^+ (2.6 to 3.5). With increased $DHNA^-$ (and Na^+) concentration, there is a more symmetric atomic density distribution (data not shown) than that at lower concentration (Model 4, Figure 3). Some aggregation of $DHNA^-$ is found away from the surface. Whereas a single Ca^{2+} ion can bind two $DHNA^-$ ions simultaneously, promoting clumping such that $DHNA^-$ (positionally described by carbon attached to the negatively charged oxygen) cannot approach the surface, a Na^+ ion neutralizes a single $DHNA^-$, resulting in a more mobile species that has greater access to the surface.

To test the effect of aqueous concentration on adsorption, an additional simulation was performed in which the concentration of $DHNA^-$ was reduced to seven anions. Surface coverage of $DHNA^-$ and Ca^{2+} decreased by at least a factor of 4 to 0.22 and 0.13, respectively. This could indicate that the simulation is not completely equilibrated because $DHNA^-$ and Ca^{2+} ions have not yet reached the surface coverage levels

DOI: 10.1021/acs.jpcc.7b06688
J. Phys. Chem. C 2017, 121, 22787−22796

found above (and the surface areas are identical). The density profiles also suggest a lack of equilibration as there is some adsorption asymmetry between the two surfaces. However, extending these simulations for an additional 10 ns did not significantly alter the density profiles or surface coverages (Figure 7).

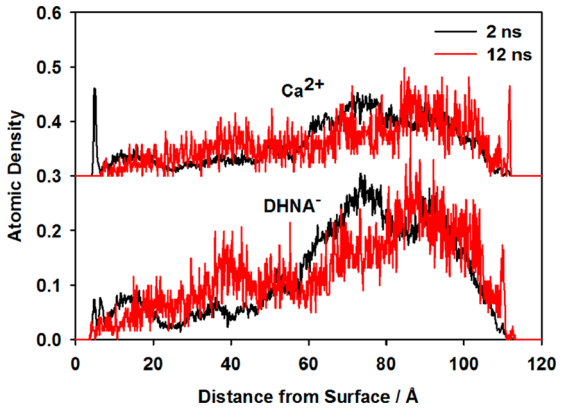

Figure 7. Surface density profiles of $DHNA^-$ and Ca^{2+} for typical 2 ns runs and extended 12 ns runs. $DHNA^-$ densities were determined from positions of carboxylate C atoms.

For charged surfaces (Models 7−15), charge-balancing Ca^{2+} ions effectively neutralize the negative kaolinite charge by adsorbing at deprotonation sites. With no $DHNA^-$ ions present, there are on average 5.5 adsorbed Ca^{2+} ions (91%) in the first adsorption layer. Deprotonation sites with adsorbed Ca^{2+} ions become net positively charged, which can then attract $DHNA^-$ ions. Similarly, Na^+ ions also adsorb at the negatively charged surface sites, with some differences compared to the Ca^{2+} case. With no $DHNA^-$ present, Table 5 shows that only 71% of Na^+ ions are adsorbed, compared to 91% of Ca^{2+} ions. However, this represents a greater coverage of deprotonation sites (71% vs 46% for Ca^{2+}). Whereas the adsorption of Ca^{2+} at the deprotonated surface results in positively charged surface sites, the adsorption of Na^+ results in neutrally charged sites. On the basis of these surface coverages with no $DHNA^-$ present, electrostatic considerations suggest that the adsorption of $DHNA^-$ at negatively charged surfaces will be greatly enhanced when Ca^{2+} ions are present to create net positively charged adsorption sites.

When Ca^{2+} ions are present in the pore, $DHNA^-$ adsorption is much greater at the deprotonated surface than at the neutral surface. The number of adsorbed $DHNA^-$ increases from 1.1 to 6.3. Figure 8a shows that Ca^{2+} bridging is the dominant mechanism for $DHNA^-$ adsorption. An average of 8.1 Ca^{2+} ions is found at the surface (68% of sites covered), many of which bridge $DHNA^-$ ions. In terms of EOR processes, molecules in the desorbed organic phase in Figure 8b would be easily recovered, while the Ca-bridged compounds would require enhanced methods for desorption and recovery. Some Ca^{2+} ions are found at the surface (primarily at negatively charged deprotonation sites) without coordinating $DHNA^-$ while other Ca^{2+} ions coordinate to desorbed $DHNA^-$ (Figure 8a). Doubling the $DHNA^-$ concentration (Model 10) significantly reduces the amount of adsorbed $DHNA^-$ due to the formation of an organic phase in the pore (Figure 8b).

Representative atomic density plots of $DHNA^-$ adsorption on negatively charges surfaces are shown in Figure 3 for each

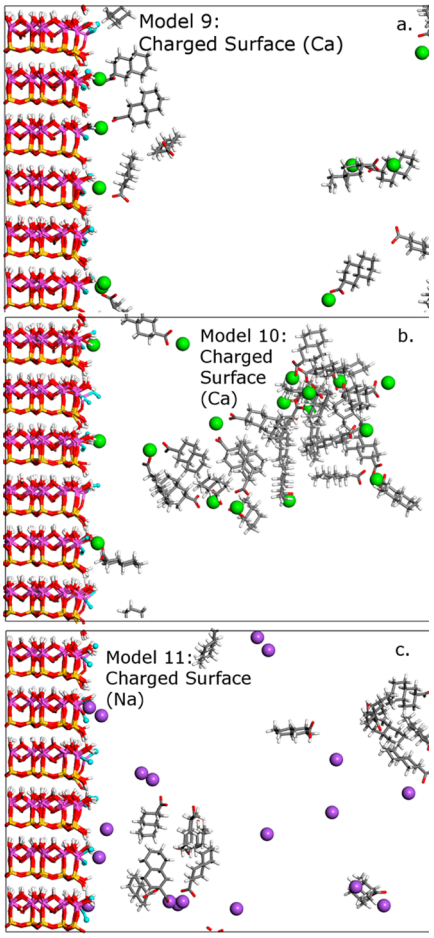

Figure 8. Representative snapshots of deprotonated surfaces: Model 9 (14 $DHNA^-$, 13 Ca^{2+} ions) (a), Model 10 (28 $DHNA^-$, 20 Ca^{2+} ions) (b), and Model 11 (14 $DHNA^-$, 26 Na^+ ions) (c). Hydroxyl atoms at deprotonation sites are colored blue. Water molecules are not displayed in the pore region for ease in viewing organic anions and counterions.

cation (Ca^{2+}, Model 9, and Na^+, Model 11). Overall, for the Ca^{2+} simulations, enhanced interactions between Ca^{2+} and deprotonated surface sites result in a shift of both Ca^{2+} and $DHNA^-$ density closer to the surface. The Ca^{2+} density plots indicate the presence of Ca^{2+} as close as 2 Å from the surface. For Na^+ simulations, deprotonation of the surface does not change the positions of Na^+ or $DHNA^-$ relative to the surface.

With Na^+ rather than Ca^{2+} in the pore, $DHNA^-$ adsorption is essentially unchanged when deprotonated surface sites are present. Na^+ ions readily adsorb at these surface sites, resulting in a neutral surface comparable to the neutral protonated surface. Although Na^+ ions are present at deprotonated surface sites, the scarcity of adsorbed $DHNA^-$ at the deprotonated surface (Table 5 and Figure 8c) indicates that Na^+ bridging is not a dominant mechanism for $DHNA^-$ adsorption. Some Na^+ bridging does occur, as evidenced by Na^+ and $DHNA^-$ atomic density peaks near the deprotonated surface (Model 11, Figure 3) and illustrated in Figure 9. In fact, most desorbed $DHNA^-$ ions are not coordinated to Na^+, while nearly all $DHNA^-$ ions are coordinated to Ca^{2+} when available (Figures 4a and 8a). As seen in Table 5, doubling the concentration of $DHNA^-$ (and Na^+) results in a small increase in adsorbed $DHNA^-$ (1.1 to 1.3, Models 11 and 12), corresponding to a small increase in adsorbed Na^+ (12.2 to 13.7). Between the two Na^+ simulations,

DOI: 10.1021/acs.jpcc.7b06688
J. Phys. Chem. C 2017, 121, 22787−22796

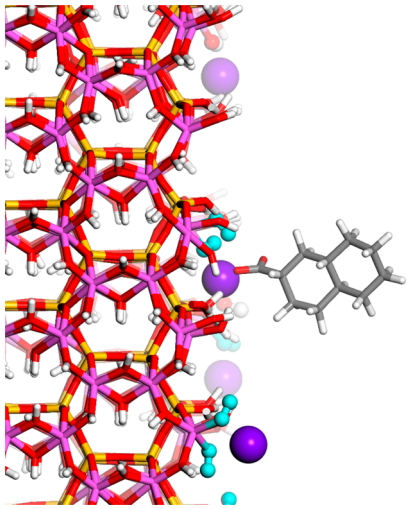

Figure 9. Snapshot of a $DHNA^-$ anion adsorbed to a deprotonated surface site via Na^+ bridging (Model 11:14 $DHNA^-$, 26 Na^+ ions). Hydroxyl atoms at deprotonation sites are colored blue. Water molecules have been removed from the pore region for ease in viewing organic anions and counterions.

the number of $DHNA^-$ ions per Na^+ at the surface is nearly constant (0.09 and 0.10).

The primary effect of introducing negatively charged deprotonation sites at the kaolinite edge is a large increase in cation adsorption (Table 5: 0.5 Ca^{2+} on the neutral surface, 8.1 Ca^{2+} on the negative surface; 2.6 Na^+ on the neutral surface, 12.2 Na^+ on the negative surface). Trends in $DHNA^-$ adsorption then follow from the availability of net positive-charged surface sites created by Ca^{2+} adsorption. As Na^+ replaces Ca^{2+} at the deprotonated surface sites, these sites become charge-neutral and less attractive for organic anions such as $DHNA^-$.

A comparison of cation coordination environments is shown in Table 6 for Ca^{2+} and Na^+. For the neutral surface, 8-fold Ca^{2+} coordination is observed, with the first shell consisting of ~4.5 O from water and ~3.5 O from $DHNA^-$ (carboxylate groups). The Ca^{2+} coordination structure indicates that these adsorbed ions remain fully hydrated as outer-sphere surface complexes. In contrast, for a deprotonated surface, hydroxyl groups at the deprotonation site contribute to the coordination of Ca^{2+}, indicative of inner-sphere Ca^{2+} surface complexes (verified by the density plots above). The contribution of $DHNA^-$ decreases from 3.5 to 1.9 (a coordination of 2 from $DHNA^-$ corresponds to a single carboxylate group) as more Ca^{2+} and $DHNA^-$ are adsorbed. Because there are now Ca^{2+} ions at the surface without associated $DHNA^-$ ions, the water contribution to the first coordination shell of Ca^{2+} increases slightly.

Sodium ions maintain 6-fold coordination regardless of surface charge or with $DHNA^-$ present. The first coordination shell consists of ~5.0 O from water, 0.7 O from $DHNA^-$, and a small amount (~0.1) from a surface hydroxyl group (due to Na^+ close to the surface). Because Na^+ is found in solution, there is a decrease in the total coordination below six when $DHNA^-$ is in solution, possibly due to the coordination of the large $DHNA^-$ ion preventing coordination of water. For the deprotonated surface, OH groups at the deprotonation site contribute an average of ~0.5 O to the coordination of Na^+. More Na^+ ions are adsorbed to the surface where $DHNA^-$ and other surface species have a greater contribution to the coordination, decreasing the contribution of water to the coordination shell.

A comparison of the observed $DHNA^-$ adsorption trends with respect to different counterions, $DHNA^-$ concentration, and surface charge state is shown in Figure 10. For Na^+ as the

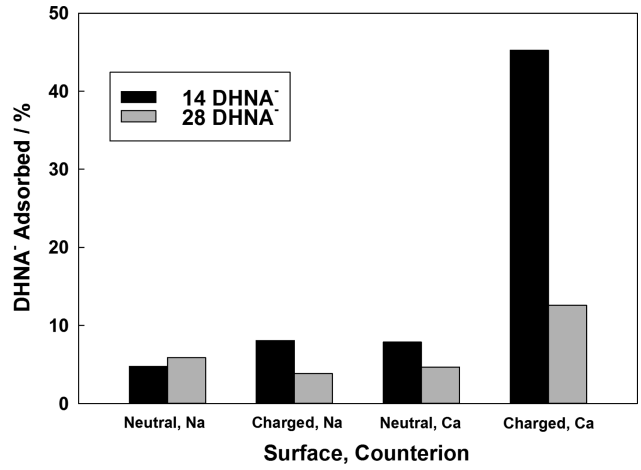

Figure 10. $DHNA^-$ adsorption for varying surface type, counterion type, and $DHNA^-$ concentration.

counterion, there is little effect on the adsorption due to $DHNA^-$ concentration or surface charge. However, for Ca^{2+}, the negatively charged surface results in increased $DHNA^-$ adsorption at both concentration levels. This may be attributed to the greater charge of Ca^{2+} compared to that of Na^+. The decrease in percent $DHNA^-$ adsorption at the higher concentration is consistent for Ca^{2+} simulations with neutral and charged surfaces and is likely associated with the clumping of Ca^{2+}-$DHNA^-$ in the aqueous solution. This response may be ultimately traced back to the competition of Ca^{2+} for negatively charged sites at the surface and with $DHNA^-$ in solution, as well as the strong repulsive electrostatics interactions among $DHNA^-$ ions. As demonstrated in Figure 10, the trend of increasing percent $DHNA^-$ adsorption with decreasing $DHNA^-$ concentration highlights the motivation for low-salinity EOR efforts. In the presence of divalent cations such as Ca^{2+}, many organic anions will be bound at such adsorption sites.

Comparisons may also be made between the percent $DHNA^-$ adsorption results at kaolinite edge surfaces from this study and the basal surfaces from our previous study.[10] Only 5% of $DHNA^-$ ions are adsorbed on the neutral edge surface in the presence of Na^+ ions, compared with 24% $DHNA^-$ adsorption on the basal (hydroxylated) kaolinite surface.[10] The basal surface has a significantly larger fraction of adsorbed Na^+ ions than the neutral edge surface, resulting in more positively charged adsorption sites for $DHNA^-$ ions. The basal surface of Ca-montmorillonite is somewhat analogous to the charged kaolinite edge surface in that both surfaces are neutralized by Ca^{2+} ions. The Ca-montmorillonite model system also included aqueous Na^+ ions to balance the organic anion charge, which is similar to the deprotonated kaolinite edge models in this study that contained both Na^+ and Ca^{2+} ions (Models 13–15). The percent $DHNA^-$ adsorption results are consistent: 27% $DHNA^-$ adsorption in the Ca-montmorillonite model[10] lies within the range of values (14–35%) for the deprotonated kaolinite models with mixed Na^+/Ca^{2+}

DOI: 10.1021/acs.jpcc.7b06688
J. Phys. Chem. C 2017, 121, 22787–22796

compositions. The key finding in both studies is that the adsorption of organic anions on hydrophilic mineral surfaces is controlled by the availability of positively charged surface sites, either by a monovalent cation at a neutral surface site or a divalent cation at a negative surface site.

5. CONCLUSIONS

Stable kaolinite (010) edge surfaces in contact with an aqueous pore containing an organic resin ($DHNA^-$) have been simulated using a flexible force field model and a deprotonation scheme that effectively removes H^+ from H_2O coordinated to surface Al sites, resulting in negatively charged surface deprotonation sites. Only the anion form of the organic resin was simulated, corresponding to a solution pH above the molecule's pK_a (approximately 4.5), which is consistent with reservoir conditions. The surface adsorptive properties of the kaolinite edge (neutral and deprotonated) have been investigated for low and high $DHNA^-$ concentrations, with Na^+ and Ca^{2+} as counterions.

The tendency of $DHNA^-$ ions to coordinate with divalent cations such as Ca^{2+} rather than monovalent ions (Na^+) greatly influences the adsorption tendencies. A clear trend of decreased $DHNA^-$ adsorption is observed as Ca^{2+} is replaced by Na^+ for deprotonated surfaces. At higher $DHNA^-$ and Ca^{2+} concentration, strong hydrophobic forces between organic species result in the formation of an organic-rich phase in solution, decreasing the number of adsorbed $DHNA^-$ ions. When Na^+ ions are present, $DHNA^-$ ions already form small clusters; therefore, increasing the ionic concentrations has little effect on the relatively low adsorption. Additionally, the formation of net positively charged surface sites due to adsorbed Ca^{2+} results in increased $DHNA^-$ adsorption. Divalent cations such as Ca^{2+} are able to efficiently bridge surface sites and organic anions. Replacing those cations with monovalent cations such as Na^+ eliminates this adsorption mechanism, resulting in reduced adsorption of the organic species. This finding is consistent with the observed trends in low-salinity water flooding experiments, and for the first time, a molecular-based description of this adsorption process has been provided.

AUTHOR INFORMATION

Corresponding Author

*E-mail: jagreat@sandia.gov.

ORCID

J. A. Greathouse: 0000-0002-4247-3362

R. T. Cygan: 0000-0003-1262-6177

Notes

The authors declare no competing financial interest.

ACKNOWLEDGMENTS

Sandia National Laboratories is a multimission laboratory managed and operated by National Technology and Engineering Solutions of Sandia, LLC., a wholly owned subsidiary of Honeywell International, Inc., for the U.S. Department of Energy's National Nuclear Security Administration under Contract DE-NA0003525. This work was funded by BP America, and BP management is thanked for permission to publish this work.

REFERENCES

(1) Sheng, J. J. Critical Review of Low-Salinity Waterflooding. *J. Pet. Sci. Eng.* **2014**, *120*, 216−224.

(2) Jerauld, G. R.; Lin, C. Y.; Webb, K. J.; Seccombe, J. C. Modeling Low-Salinity Waterflooding. *SPE Reserv. Eval. Eng.* **2008**, *11*, 1000−1012.

(3) Mahani, H.; Berg, S.; Ilic, D.; Bartels, W. B.; Joekar-Niasar, V. Kinetics of Low-Salinity-Flooding Effect. *SPE J.* **2015**, *20*, 008.

(4) Tang, G. Q.; Morrow, N. R. Influence of Brine Composition and Fines Migration on Crude Oil/Brine/Rock Interactions and Oil Recovery. *J. Pet. Sci. Eng.* **1999**, *24*, 99−111.

(5) Teich-McGoldrick, S. L.; Greathouse, J. A.; Cygan, R. T. Molecular Dynamics Simulations of Uranyl Adsorption and Structure on the Basal Surface of Muscovite. *Mol. Simul.* **2014**, *40*, 610−617.

(6) Greathouse, J. A.; Cygan, R. T. Water Structure and Aqueous Uranyl(VI) Adsorption Equilibria onto External Surfaces of Beidellite, Montmorillonite, and Pyrophyllite: Results from Molecular Simulations. *Environ. Sci. Technol.* **2006**, *40*, 3865−3871.

(7) Kremleva, A.; Kruger, S.; Rosch, N. Uranyl Adsorption at Solvated Edge Surfaces of 2:1 Smectites. A Density Functional Study. *Phys. Chem. Chem. Phys.* **2015**, *17*, 13757−13768.

(8) Kremleva, A.; Krüger, S.; Rösch, N. Uranyl Adsorption at (0 1 0) Edge Surfaces of Kaolinite: A Density Functional Study. *Geochim. Cosmochim. Acta* **2011**, *75*, 706−718.

(9) Underwood, T.; Erastova, V.; Cubillas, P.; Greenwell, H. C. Molecular Dynamic Simulations of Montmorillonite−Organic Interactions under Varying Salinity: An Insight into Enhanced Oil Recovery. *J. Phys. Chem. C* **2015**, *119*, 7282−7294.

(10) Greathouse, J. A.; Cygan, R. T.; Fredrich, J. T.; Jerauld, G. R. Adsorption of Aqueous Crude Oil Components on the Basal Surfaces of Clay Minerals: Molecular Simulations Including Salinity and Temperature Effects. *J. Phys. Chem. C* **2017**, DOI: 10.1021/acs.jpcc.7b06454.

(11) Churakov, S. V. Ab Initio Study of Sorption on Pyrophyllite: Structure and Acidity of the Edge Sites. *J. Phys. Chem. B* **2006**, *110*, 4135−4146.

(12) Churakov, S. V. Structure and Dynamics of the Water Films Confined between Edges of Pyrophyllite: A First Principle Study. *Geochim. Cosmochim. Acta* **2007**, *71*, 1130−1144.

(13) Liu, X.; Lu, X.; Wang, R.; Meijer, E. J.; Zhou, H.; He, H. Atomic Scale Structures of Interfaces between Kaolinite Edges and Water. *Geochim. Cosmochim. Acta* **2012**, *92*, 233−242.

(14) Liu, X.; Lu, X.; Meijer, E. J.; Wang, R.; Zhou, H. Atomic-Scale Structures of Interfaces between Phyllosilicate Edges and Water. *Geochim. Cosmochim. Acta* **2012**, *81*, 56−68.

(15) Tazi, S.; Rotenberg, B.; Salanne, M.; Sprik, M.; Sulpizi, M. Absolute Acidity of Clay Edge Sites from Ab-Initio Simulations. *Geochim. Cosmochim. Acta* **2012**, *94*, 1−11.

(16) Suter, J. L.; Kabalan, L.; Khader, M.; Coveney, P. V. Ab Initio Molecular Dynamics Study of the Interlayer and Micropore Structure of Aqueous Montmorillonite Clays. *Geochim. Cosmochim. Acta* **2015**, *169*, 17−29.

(17) Zeitler, T. R.; Greathouse, J. A.; Gale, J. D.; Cygan, R. T. Vibrational Analysis of Brucite Surfaces and the Development of an Improved Force Field for Molecular Simulation of Interfaces. *J. Phys. Chem. C* **2014**, *118*, 7946−7953.

(18) Martins, D. M. S.; Molinari, M.; Gonçalves, M. A.; Mirão, J. P.; Parker, S. C. Toward Modeling Clay Mineral Nanoparticles: The Edge Surfaces of Pyrophyllite and Their Interaction with Water. *J. Phys. Chem. C* **2014**, *118*, 27308−27317.

(19) Yu, K.; Schmidt, J. R. Elucidating the Crystal Face- and Hydration-Dependent Catalytic Activity of Hydrotalcites in Biodiesel Production. *J. Phys. Chem. C* **2011**, *115*, 1887−1898.

(20) White, G. N.; Zelazny, L. W. Analysis and Implications of the Edge Structure of Dioctahedral Phyllosilicates. *Clays Clay Miner.* **1988**, *36*, 141−146.

(21) Bickmore, B. R.; Rosso, K. M.; Nagy, K. L.; Cygan, R. T.; Tadanier, C. J. Ab Initio Determination of Edge Surface Structures for Dioctahedral 2:1 Phyllosilicates: Implications for Acid-Base Reactivity. *Clays Clay Miner.* **2003**, *51*, 359−371.

DOI: 10.1021/acs.jpcc.7b06688
J. Phys. Chem. C 2017, 121, 22787−22796

(22) Aitken, C. M.; Jones, D. M.; Larter, S. R. Anaerobic Hydrocarbon Biodegradation in Deep Subsurface Oil Reservoirs. *Nature* **2004**, *431*, 291−294.
(23) Bish, D. L. Rietveld Refinement of the Kaolinite Structure at 1.5 K. *Clays Clay Miner.* **1993**, *41*, 738−744.
(24) Cygan, R. T.; Liang, J.-J.; Kalinichev, A. G. Molecular Models of Hydroxide, Oxyhydroxide, and Clay Phases and the Development of a General Force Field. *J. Phys. Chem. B* **2004**, *108*, 1255−1266.
(25) Greathouse, J. A.; Durkin, J. S.; Larentzos, J. P.; Cygan, R. T. Implementation of a Morse Potential to Model Hydroxyl Behavior in Layered Aluminosilicates. *J. Chem. Phys.* **2009**, *130*, 134713.
(26) Dauber-Osguthorpe, P.; Roberts, V. A.; Osguthorpe, D. J.; Wolff, J.; Genest, M.; Hagler, A. T. Structure and Energetics of Ligand-Binding to Proteins - Escherichia-Coli Dihydrofolate Reductase Trimethoprim, a Drug-Receptor System. *Proteins: Struct., Funct., Genet.* **1988**, *4*, 31−47.
(27) Brady, P. V.; Cygan, R. T.; Nagy, K. L. Molecular Controls on Kaolinite Surface Charge. *J. Colloid Interface Sci.* **1996**, *183*, 356−364.
(28) Liu, X. D.; Lu, X. C.; Sprik, M.; Cheng, J.; Meijer, E. J.; Wang, R. C. Acidity of Edge Surface Sites of Montmorillonite and Kaolinite. *Geochim. Cosmochim. Acta* **2013**, *117*, 180−190.
(29) Brady, P. V.; Krumhansl, J. L. A Surface Complexation Model of Oil−Brine−Sandstone Interfaces at 100°C: Low Salinity Waterflooding. *J. Pet. Sci. Eng.* **2012**, *81*, 171−176.
(30) Plimpton, S. Fast Parallel Algorithms for Short-Range Molecular Dynamics. *J. Comput. Phys.* **1995**, *117*, 1−19.
(31) Teleman, O.; Jonsson, B.; Engstrom, S. A Molecular-Dynamics Simulation of a Water Model with Intramolecular Degrees of Freedom. *Mol. Phys.* **1987**, *60*, 193−203.

DOI: 10.1021/acs.jpcc.7b06688
J. Phys. Chem. C 2017, 121, 22787−22796